Suppressing Wall Turbulence by Means of a Transverse Traveling Wave

Yiqing Du[1] and George Em Karniadakis[2]*

Direct numerical simulations of wall-bounded flow reveal that turbulence production can be suppressed by a transverse traveling wave. Flow visualizations show that the near-wall streaks are eliminated, in contrast to other turbulence-control techniques, leading to a large shear stress reduction. The traveling wave can be induced by a spanwise force that is confined within the viscous sublayer; it has its maximum at the wall and decays exponentially away from it. We demonstrate the application of this approach in salt water, using arrays of electromagnetic tiles that produce the required traveling wave excitation at a high efficiency.

The control of wall-bounded flows in an effort to reduce viscous stresses has been studied since Prandtl first used a trip wire to trigger transition in the boundary layer. Since then, a wide variety of experimental and numerical studies have been performed to determine efficient and feasible control mechanisms for wall shear stress modification (*1*, *2*). The development of turbulence-control mechanisms and corresponding shear stress modification depends on the observations that organized structures in the near-wall turbulence and friction drag are linked (*3*). Turbulent boundary layers typically contain low-speed streaks (*4*) and stable three-dimensional vortical structures, called hairpins (*5–7*). Our numerical simulations confirm these experimental findings (Fig. 1).

Most turbulence-control methods have been developed under the assumption that the turbulence production cycle could be favorably altered, stabilized, or reduced in intensity by the manipulation and alteration of low-speed streaks, quasi-streamwise vortices, the viscous sublayer, or the hairpin-like structures that populate the near-wall region. The use of small grooves or riblets on the wall surface has been shown to suppress turbulence and reduce the drag force by about 5 to 10% (*8*, *9*). We can also imagine the use of applied near-wall forces that would act to redistribute the streamwise vorticity present in hairpinlike structures in an effort to modify the shear stress and turbulent momentum transport at the wall.
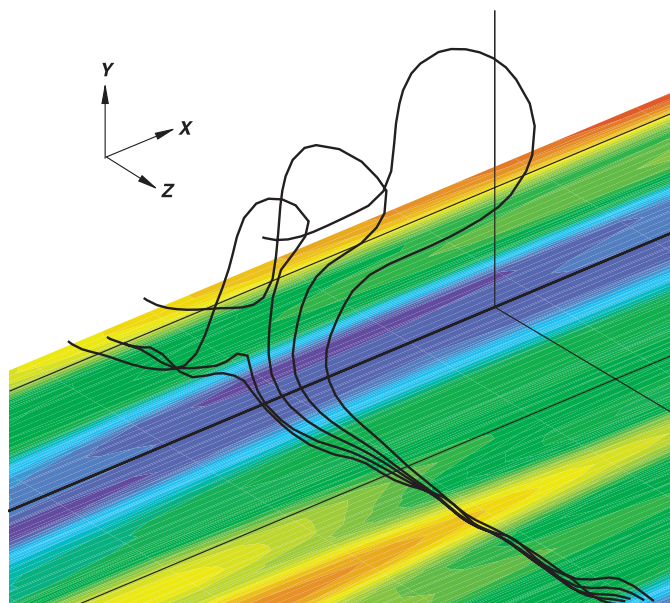
In this report, we show that application of a force along the spanwise direction, within the viscous sublayer and decaying exponentially away from the wall, can reduce turbulence. In particular, we use the traveling wave force (F_z)

$$F_z = Ie^{-y/\Delta} \sin\left(\frac{2\pi}{\lambda_z} z - \frac{2\pi}{T} t \right) \quad (1)$$

where I is the amplitude of excitation, Δ is the penetration length, λ_z is the wavelength (along the span), T is the time period, and t is time. Here $\Delta^+ = u_*\Delta/\nu \approx 5$ (nondimensional, in wall units), where u_* is the wall shear velocity and ν is the kinematic viscosity. We first studied the numerical models, in which the computational domain is a channel and the force is acting on the lower wall while the upper wall is unaffected. All parameters in Eq. 1, i.e., (I, T, λ_z), are nondimensionalized with respect to the channel half-width and the center line velocity. The Reynolds number Re_* is about 150 (based on the wall shear velocity u_* and the channel half-width). The size of the computational domain is $L_x = 2100$ by $L_y = 300$ by $L_z = 840$ in wall units, in the streamwise, normal, and spanwise directions, respectively; periodicity is assumed to be along the streamwise and spanwise directions. The discretization is performed with spectral/hp element methods with the code $\mathcal{N}\varepsilon\kappa\tau\alpha r$ (*10*).

The traveling wave, when it is effective in reducing the drag force on the controlled wall, weakens and in many cases eliminates completely the wall streaks (Fig. 2). The upper wall exhibited the familiar turbulence structure consisting of pairs of high-speed and low-speed streaks with the characteristic spacing of about 100 wall units, but no such pairs were found near the controlled surface (*11*). Instead, a wide ribbon of low-speed velocity formed in the region where the streamwise vorticity achieves positive values at the same instant. Streaks and streak spacing are usually difficult to alter even in cases where a large amount (e.g., 50%) of drag reduction has been obtained (*12*).

In contrast, streamwise riblets produced a drag reduction of only 5% (*13*); although the lateral spacing of the streaks did not change, the streaks appeared more elongated compared with the uncontrolled case (Fig. 3). A larger amount of drag reduction was achieved in the so-called "vee design," and the spacing of the streaks increased by about 10% (*14*). If instead of a traveling wave an oscillatory flow along the spanwise direction is imposed by a force similar to the one described in Eq. 1 [inspired by the work in (*15*)], a better drag reduction of 30% is achieved at the optimum period $T^+ \approx 100$. However, the wall streaks are still present (Fig. 4), but they are inclined with respect to the flow direction because of

Fig. 1. Hairpin-like structures and instantaneous streamwise velocity contours for turbulent flow over a smooth wall ($Re_\tau \approx 150$). Blue indicates low-speed streaks and red indicates high-speed streaks; green corresponds to average velocity values. The black lines denote vortex lines. Only a small portion of the domain is shown for clarity, containing a pair of low- and high-speed streaks. This and similar pictures in the entire domain show that near-wall turbulence is populated with hairpin-like structures and that low-speed streaks are located between the "legs" of these structures.

[1]Department of Mechanical Engineering, Massachusetts Institute of Technology, Cambridge, MA 02139, USA. [2]Division of Applied Mathematics, Brown University, Providence, RI 02912, USA.

*To whom correspondence should be addressed.

the spanwise flow component. In both cases, despite these obvious modifications, the fundamental structure of near-wall streaks and hairpins remains the same, unlike in the traveling wave excitation, where no wall streaks or hairpin vortices can be found.

The specific waveform, i.e., the parameters T, λ_z, and I, is critical in obtaining turbulence suppression and, correspondingly, drag reduction. For example, for cases with $I = 1$, $\lambda_z^+ = 840$, and $T^+ = 100$, 50, and 25, drag reduction was about 30% for $T^+ = 50$ and 15% for $T^+ = 25$, whereas the drag force increased for $T^+ = 100$. This last result is surprising if we compare it with the oscillatory flow along the span. In the latter case, the time period $T^+ \approx 100$ leads to the largest amount of drag reduction, whereas in the traveling wave case, $T^+ = 50$ gives the maximum drag reduction among the three cases. The underlying mechanisms are fundamentally different between the two cases. In the former case, the reduction is related to the action of the Stokes layer (15), whereas in the latter case, it can be explained with the stabilization of the near-wall streaks and regeneration mechanisms of near-wall turbulence (16, 17). Another substantial difference between these two cases is that in oscillatory flow, the amount of drag reduction is increased as the amplitude of excitation I increases, unlike in the traveling wave excitation.

The finding regarding the amplitude suggests that the energetics are more favorable for the traveling wave excitation. Furthermore, we found that it is the total amount of energy input that is critical in suppressing turbulence, and this can be expressed by the product $I \cdot T^+$. Evidence for such a criterion is provided in Fig. 5, where we plot the time history of drag force normalized with its initial no-control value and the normalized drag force on the upper (no-control) wall, which oscillates around unity. In the plot, the curve that corresponds to $T^+ = 50$ and $I = 0.5$ is close to the curve corresponding to $T^+ = 25$ and $I = 1$, and both curves are for the same total energy input. To further test this hypothesis, we set $I = 2$ for $T^+ = 25$ and $I = 1$ for $T^+ = 50$ at time = 50 and continue the simulation. Now both cases have the same energy input as the case shown by the lowest curve in the plot, which corresponds to $I = 1$ and $T^+ = 50$. We can see that there is a sudden decrease in the drag force at the beginning, and eventually both curves follow each other closely toward the lowest curve in the plot. Of course, not every combination of (I, T^+) will result in drag reduction. For example, we carried out a simulation with $I = 0.25$ and $T^+ = 200$ that led to a drag increase. This means that we first have to find the appropriate range of frequency, and subsequently we have to optimize the efficiency of this control mechanism.

In applications, it is not always possible to induce a perfect wave. Moreover, it is better to produce a traveling wave motion by discrete actuators that are sparsely distributed on the wall surface (18). In these cases, it is clear that an approximate traveling wave is produced, and the question is if such nonideal excitation also suppresses wall turbulence. We performed several computational experiments to investigate this question (11). We obtained the same result, i.e., drag was reduced by more than 30%, but the excitation frequency needed to be higher as the "effective" wavelength is smaller. This, in turn, suggests that the phase speed of the traveling wave is important, in that it has to be above a certain value, e.g., at least one-third of the free-stream velocity, in order to be effective in suppressing turbulence.

Another parameter that determines the net amount of drag reduction is the penetration length Δ in Eq. 1. By increasing its value, a larger amount of drag reduction is achieved (more than 50% for $\Delta^+ \approx 10$), but for Δ much larger than the viscous sublayer, a drag increase has been observed. This relatively small penetration of the excitation force into
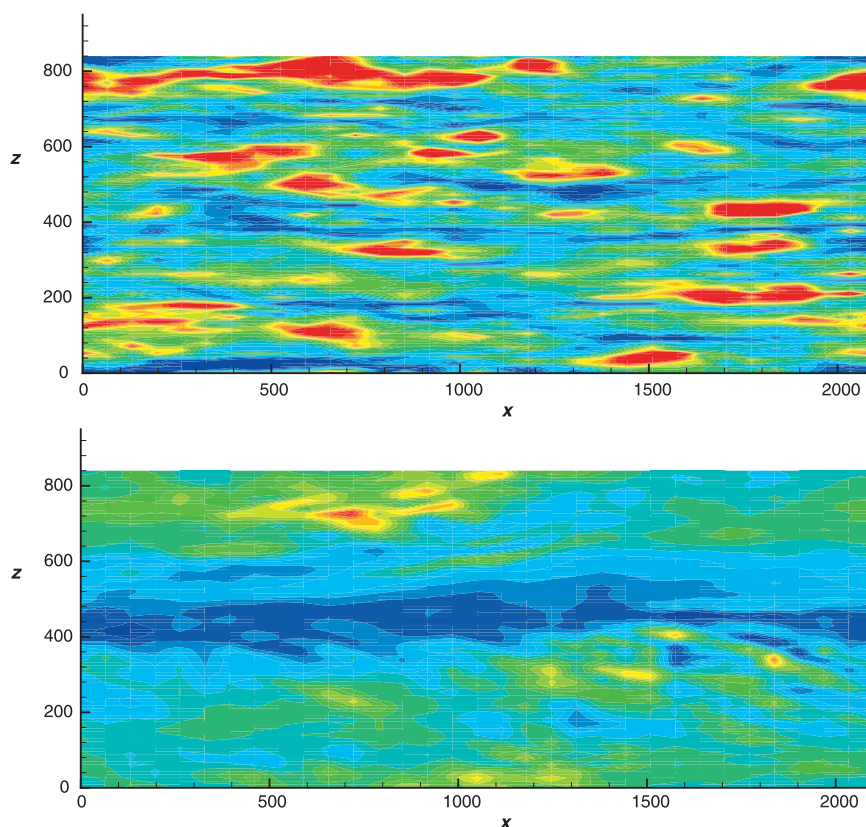

Fig. 2. Instantaneous flow visualizations of wall streaks. (**top**) No control. (**bottom**) Traveling wave excitation corresponding to $I = 1$, $\lambda_z^+ = 840$, and $T^+ = 50$; $L_z^+ = 840$. Blue indicates low-speed streaks and yellow-red indicates high-speed streaks.
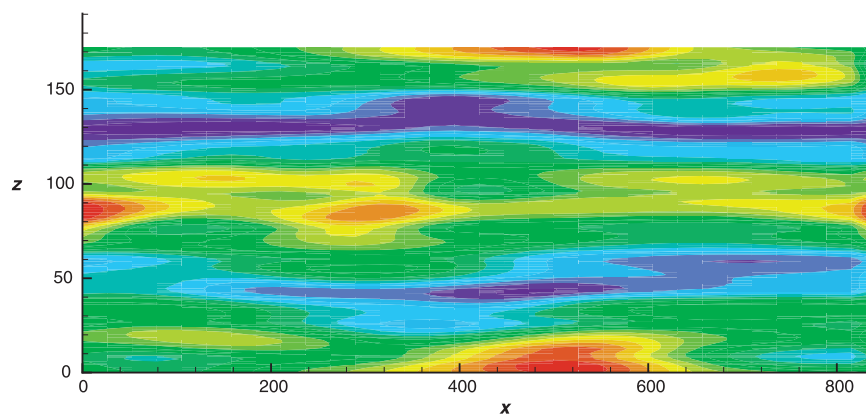

Fig. 3. Instantaneous streamwise velocity contours near a wall with riblets. $L_z^+ = 200$. Blue indicates low-speed streaks and yellow-red indicates high-speed streaks.

the fluid suggests several surface-based techniques as cost-effective actuation candidates. Moreover, the simulations show that large values of the amplitude I are not necessary to obtain drag reduction. For example, at a period $T^+ = 100$, excitations with $I = 1$ and $I = 2$ led to drag increase, but $I = 0.5$ led to drag decrease. Also, the characteristic length scale here is on the order of tens of wall-streak spacing, i.e., 1000 wall units or more. Indeed, the simulation results suggest a monotonic increase in the amount of drag reduction in the wavelength range tested from $\lambda_z^+ = 210$ to $\lambda_z^+ = 840$ (*11*).

As a test, first consider flow around a remotely operated vehicle (ROV) with a typical Reynolds number of 1,000,000 and a boundary layer thickness of 5 mm. On the basis of the set of nondimensional parameters obtained in the simulation, an appropriate range for the dimensional wavelength and pulsing frequency is 20 mm and 50 Hz, respectively. For submarines with typical Reynolds number of 100,000,000, the required wavelength is about 2 mm and the frequency is 5 kHz. For aerodynamic applications at similar conditions, the wavelength is an order of magnitude larger and the frequency an order of magnitude lower. These values suggest that the proposed method can be implemented by a variety of techniques, especially in the context of emerging micro-electromechanical systems (MEMS) technologies (*18*), i.e., by means of microactuators or by means of morphing surfaces. A morphing surface involves the creation of smart skin that can be cast and pasted on existing vehicles with minimal intrusion. This smart skin contains actuators of small size and substantial force, such as piezoceramic and magnetostrictive materials (*19*) as well as shape memory alloys (SMA) (*20*). Piezoceramic actuators can produce up to 1-cm displacement and respond up to a frequency of 20 kHz at a driving voltage of 100 V. Therefore, they are more appropriate in the high–Reynolds number regime. SMAs are more efficient and work well in the lower Reynolds number regime as in ROV applications; these have been successfully demonstrated (*20*). For a strip width of 10 cm, a single SMA wire of less than 1 mm producing a force of 20N is sufficient to produce the desired traveling wave pattern. The overall efficiency of piezoelectric or SMA actuation is not known, but in general the latter requires lower driving voltages.

A clearer demonstration of the generation of traveling waves and their effect has been provided in another experiment, in which small tiles consisting of permanent magnets and electrodes of variable polarity were mounted on the controlled surface (*21–23*). These tiles produce a three-dimensional Lorentz force, which can be directed to cause

the required spanwise excitation. We performed several simulations of different versions of this experiment (*11*). The working medium was salt water, which is a weak electric conductor, and therefore the induced electric and magnetic fields are negligible (*24*, *25*). We placed several electromagnetic tile units consisting of two electrodes and two magnets perpendicular to the flow to cover the controlled region of a flat plate (Fig. 6).

The pulsing strategy was an elaborate 16-phase scheme. Specifically, the 16 phases can be classified into two categories, each having eight phases. We refer to them as "class I" and "class II" phases. In class I, the negative electrodes are aligned in the streamwise direction, and in class II, the positive electrodes are aligned in the streamwise direction. Each subsequent phase in both classes shifts the entire pattern one electrode over in the positive spanwise z direction. The 16-phase puls-

ing pattern is formed by taking two consecutive phases in each class alternatively. First, we take the first two phases in class I, followed by the first two phases in class II; then, we take the next two phases in class I, and so on (*11*). The magnetic field was 0.5 T, the electric field was 100 V/m, the phase frequency was 3.5 Hz, and the free-stream velocity was 0.2 m/s (the boundary layer was tripped). This type of multiphase excitation generated a transverse traveling wave (Fig. 6).

The overall drag force depends on the three-dimensional distribution of the Lorentz force, which in turn relates to the geometry of the tiles (*11*). The penetration length Δ is proportional to the electrodes' width, and square type electrodes give rise to a substantial streamwise Lorentz force component equal in magnitude to the spanwise component (*11*). This streamwise force acts in com-
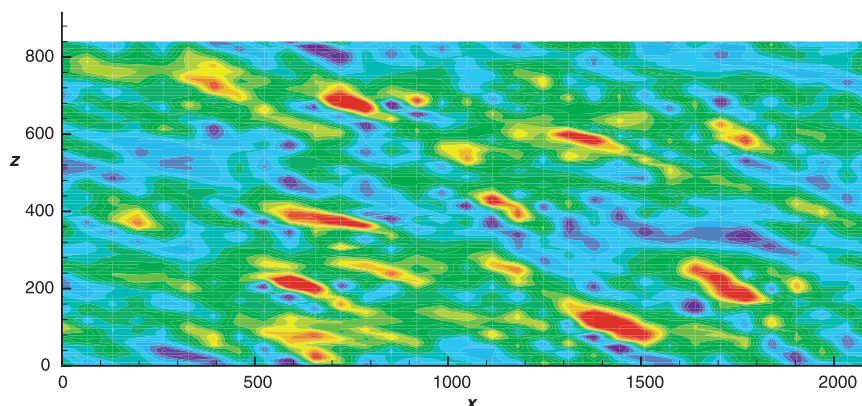

Fig. 4. Streamwise velocity contours near a wall controlled by an oscillatory force along the spanwise direction; $T^+ = 100$. $L_z^+ = 840$. Blue indicates low-speed streaks and yellow-red indicates high-speed streaks.
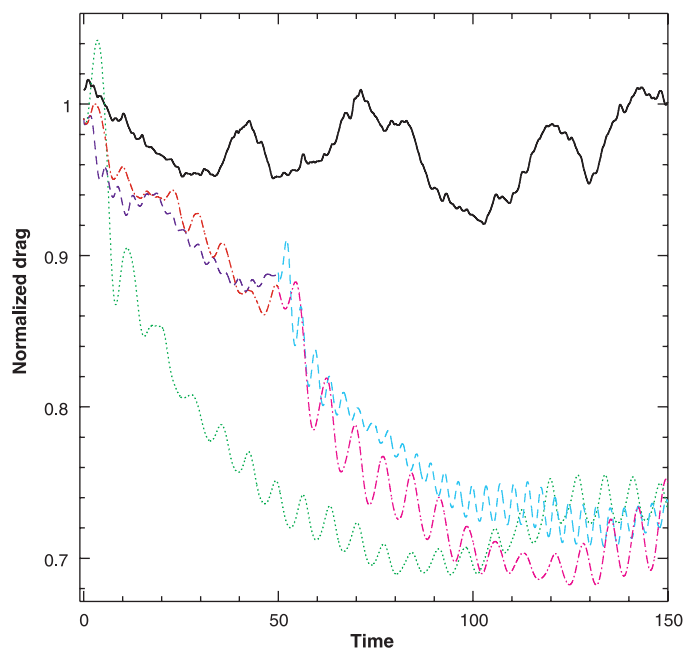

Fig. 5. Time history of normalized drag force for $\lambda_z^+ = 840$. The no-control value of the drag is used in the nondimensionalization, and time is in convective units. Black line corresponds to no control, green line to $I = 1$; $T^+ = 50$, red line to $I = 0.5$; $T^+ = 50$, pink line to $I = 1$; $T^+ = 50$, blue line to $I = 1$; $T^+ = 25$, and cyan line to $I = 2$; $T^+ = 25$.

petition with the spanwise component (*24*, *25*), and thus a net drag reduction may not be realized for some tile configurations. This is the case, for example, for the tile configuration of Fig. 6, where very small or no drag reduction was observed, in agreement with recent experiments (*23*). However, if the streamwise component is turned off in the simulation, then drag reduction is obtained. The normal force component is weaker and its effect is not substan-

tial. These results suggest a new design for an effective electromagnetic tile configuration. Specifically, we need to redesign the electrodes so that they are elongated in the spanwise direction with an aspect ratio of about 10 or higher. Simulations based on Maxwell's equations of this new configuration show a dominant spanwise Lorentz force component of the type described by Eq. 1.

To assess the overall efficiency of the pro-

posed drag reduction technique, we need to compute the power saved, P^s, and the power used, P^d; the latter is required to produce a spanwise force as described in Eq. 1. First, the power saved normalized with respect to the power of the wall shear velocity is

$$P^s = \frac{C_{\text{skin}}\rho u_*^2 UA}{\rho u_*^3 A} = C_{\text{skin}}\frac{U}{u_*} \quad (2)$$

where C_{skin} is the percentage of the drag reduction, A is the surface area, U is the free-stream velocity, and ρ is the density. To obtain an estimate for P^d, we consider the aforementioned experiment with the electromagnetic tiles. Here,

$$P^d = \frac{C_{\text{phase}}VI_{\text{eff}}}{\rho u_*^3 A} \quad (3)$$

where V is the voltage and I_{eff} is the effective current through the electrode area A_e and is proportional to the current density J. C_{phase} is a coefficient (less than unity) determined by the multiphase pattern. The current density can be computed from the amplitude I (see Eq. 1), which can be interpreted here as the interaction parameter, i.e., $I = \sigma BEL/(\rho U^2)$, where $B \approx 0.5$ T and $E \approx 100$ V/m are the magnetic and electric fields, respectively, and L is a length scale. Using these equations for the power and using the velocity in the experiment of about 0.2 m/s, we obtain the values of (normalized) saved power $P^s \approx 5$ and the value of (normalized) energy spent $P^d \approx 1$. This value is obtained with an electrode area less than 10% of the total area and for $C_{\text{phase}} = 1/16$. The favorable comparison between the power saved and the power spent suggests that electromagnetic excitation with discrete tiles and an open-loop multiphase pulsing pattern can be an efficient way of suppressing wall turbulence and obtaining substantial drag reduction.
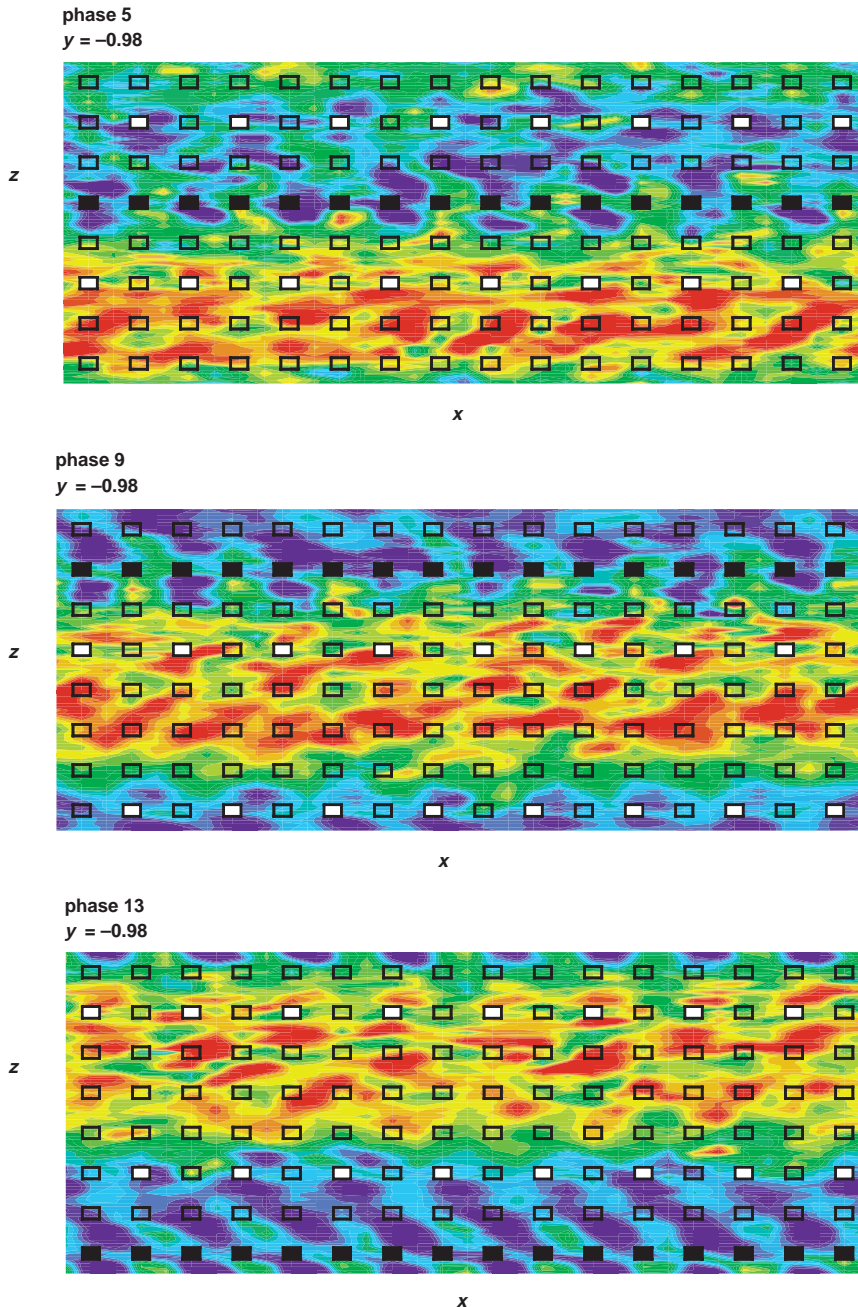

Fig. 6. Plan view of controlled wall with array of electromagnetic tiles. The electrodes are 0.3 in by 0.2 in and are placed 0.5 in apart. Shown are contours of spanwise velocity ($y^+ = 3$) taken at the end of phases 5, 9, and 13 of the excitation cycle. A periodic spanwise motion is induced by the electromagnetic pulsing. The rectangles denote the location of electrodes, with black rectangles denoting negative charge and white rectangles denoting positive charge. The rest of the electrodes are nonactive at that time instant. Red denotes flow in the positive spanwise direction and blue denotes flow in the negative spanwise direction.

References and Notes

1. M. Gad-el-Hak, *Flow Control: Passive, Active and Reactive Flow Management* (Cambridge Univ. Press, London, 2000).
2. E. Coustols and A. M. Savill, paper presented at Turbulent Skin Friction Drag Reduction by Active and Passive Means, AGARD FDP/VKI Special Course on Skin Friction and Drag Reduction, Brussels, Belgium, 2 to 6 March 1992.
3. A. A. Townsend, *The Structure of Turbulent Shear Flow* (Cambridge Univ. Press, New York, 1976).
4. S. J. Kline, W. C. Reynolds, F. A. Schraub, P. W. Runstadler, *J. Fluid Mech.* **95**, 741 (1967).
5. M. R. Head and P. R. Bandyopadhyay, *J. Fluid Mech.* **107**, 297 (1981).
6. J. M. Wallace, *Dev. Theor. Appl. Mech.* **XI**, 509 (1982).
7. A. E. Perry and M. S. Chong, *J. Fluid Mech.* **119**, 173 (1982).
8. D. W. Bechert and M. Bartenwerfer, *J. Fluid Mech.* **206**, 105 (1989).
9. K. S. Choi, *J. Fluid Mech.* **208**, 417 (1989).
10. G. E. Karniadakis and S. J. Sherwin, *Spectral/hp Elements Methods for CFD* (Oxford Univ. Press, New York, 1999), chap. 9, pp. 276–290.
11. Y. Du, thesis, Brown University, Providence, RI (1999).
12. F. Nieuwstadt and K.-S. Choi, *Lecture Notes for the Course Turbulence Modulation and Control* (Springer-Verlag, Berlin, 2000).

13. D. C. Chu and G. E. Karniadakis, *J. Fluid Mech.* **250**, 1 (1993).
14. L. Sirovich and S. Karlsson, *Nature* **388**, 753 (1997).
15. W. J. Jung, N. Mangiavacchi, R. Akhavan, *Phys. Fluids* **4**, 1605 (1992).
16. W. Schoppa and F. Hussain, in *Proceedings on Self-Sustaining Mechanics of Wall Turbulence*, R. Panton, Ed. (Computational Mechanics Publications, Billerica, MA, 1997), pp. 385–422.
17. F. Wallefe, *Phys. Fluids* **9**, 883 (1997).
18. C.-M. Ho and Y.-C. Tai, *J. Fluids Eng.* **118**, 437 (1996).
19. C. D. Near, *Proc. SPIE* **2717**, 246 (1996).
20. O. K. Rediniotis, D. C. Lagoudas, L. N. Wilson, *AIAA*

Paper No. AIAA 2000-0522 (American Institute of Aeronautics and Astronautics, Reston, VA, 2000).
21. D. Nosenchuck and G. L. Brown, in *International Conference on Near-Wall Turbulent Flows*, C. G. Speziale and B. E. Launder, Eds. (Elsevier, Amsterdam, 1993), pp. 689–698.
22. D. Nosenchuck, in *Proceedings of ASME Fluid Engineering Meeting* (American Society of Mechanical Engineers, New York, 1996), pp. 1–9.
23. D. Nosenchuck, private communication; R. Philips, private communication.
24. C. H. Crawford and G. E. Karniadakis, *Phys. Fluids* **9**, 788 (1997).
25. C. Henoch and J. Stace, *Phys. Fluids* **7**, 1371 (1995).

The Spin Excitation Spectrum in Superconducting YBa₂Cu₃O₆.₈₅

P. Bourges,[1]* Y. Sidis,[1] H. F. Fong,[2] L. P. Regnault,[3] J. Bossy,[4] A. Ivanov,[5] B. Keimer[2,6]

A comprehensive inelastic neutron scattering study of magnetic excitations in the near optimally doped high-temperature superconductor $YBa_2Cu_3O_{6.85}$ is presented. The spin correlations in the normal state are commensurate with the crystal lattice, and the intensity is peaked around the wave vector characterizing the antiferromagnetic state of the insulating precursor, $YBa_2Cu_3O_6$. Profound modifications of the spin excitation spectrum appear abruptly below the superconducting transition temperature T_c, where a commensurate resonant mode and a set of weaker incommensurate peaks develop. The data are consistent with models that are based on an underlying two-dimensional Fermi surface, predicting a continuous, downward dispersion relation connecting the resonant mode and the incommensurate excitations. The magnetic incommensurability in the $YBa_2Cu_3O_{6+x}$ system is thus not simply related to that of another high-temperature superconductor, $La_{2-x}Sr_xCuO_4$, where incommensurate peaks persist well above T_c. The temperature-dependent incommensurability is difficult to reconcile with interpretations based on charge stripe formation in $YBa_2Cu_3O_{6+x}$ near optimum doping.

Electronic conduction in the high-temperature superconductor cuprate takes place predominantly in CuO₂ layers. Most theories therefore regard the electronic state that forms the basis of high-temperature superconductivity as an essentially two-dimensional (2D) strongly correlated metal. The CuO₂ sheets in one family of copper oxides ($La_{2-x}Sr_xCuO_4$) have, however, been shown to be unstable against the formation of 1D "charge stripes" (*1*), even near doping levels where the superconducting transition temperature T_c is maximum. This observation has boosted models in which the underlying electronic instability is 1D and the formation of

(static or fluctuating) stripes is an essential precondition for high-temperature superconductivity [see, e.g., (*2*)]. However, $La_{2-x}Sr_xCuO_4$ has some low-energy phonon modes conducive to stripe formation that are not generic to the high-T_c compounds, and the maximum T_c in this system is anomalously low. It is therefore important to test whether stripe-based scenarios are viable in other cuprates with higher T_c, where this lattice dynamical peculiarity is not present.

The most salient signature of charge stripes is an associated (static or dynamic) spin density modulation that can be detected by neutron scattering. In $La_{2-x}Sr_xCuO_4$, this modulation manifests itself as four well-defined incommensurate peaks at wave vectors $Q_\delta = (\pi(1 \pm \delta), \pi)$ and $(\pi, \pi(1 \pm \delta))$ (in square lattice notation with unit lattice constant; δ is the incommensurability parameter) in the magnetic spectrum (*3–6*), which are interpreted as arising from two 1D domains. Neutron scattering experiments on the $YBa_2Cu_3O_{6+x}$ system have, however, revealed excitations that are peaked at $Q_{AF} = (\pi, \pi)$ (*7–13*), the ordering wave vector of the 2D antiferromagnetic state observed when

the doping level is reduced to zero. In particular, the commensurate "resonance peak" at (π, π) that dominates the spectrum in the superconducting state (*9–15*) is difficult to reconcile with scenarios based on fluctuating 1D domains incommensurate with the host lattice. Recently, an incommensurate pattern with a fourfold symmetry reminiscent of $La_{2-x}Sr_xCuO_4$ has also been discovered in some constant-energy cuts of the magnetic spectrum of underdoped $YBa_2Cu_3O_{6.6}$ (*16–18*), which was taken as experimental support for stripe-based scenarios of superconductivity. We report a neutron scattering study of near optimally doped $YBa_2Cu_3O_{6.85}$ ($T_c = 89$ K), demonstrating that (unlike in $La_{2-x}Sr_xCuO_4$) the incommensurate pattern appears only below T_c. Magnetic excitations in the normal state are commensurate and centered at $Q = (\pi, \pi)$. Our data are consistent with 2D Fermi liquid–like theories (not invoking stripes) (*19–23*) and especially that which predicts a continuous, downward dispersion of the magnetic resonance peak (*20*).

The experiments were performed on a large twinned single crystal (mass of ~9.5 g) grown using the top seed melt texturing method (*24*). The sample was subsequently annealed in oxygen and displays a sharp superconducting transition (T_c) at 89 K measured by a neutron depolarization technique that is sensitive to the entire bulk (*24*). Experiments were carried out on two triple-axis spectrometers: IN8 at the Institut Laue-Langevin, Grenoble (France), and 2T at the Laboratoire Léon Brillouin, Saclay (France) (*25*). Two different scattering geometries were used on both spectrometers. On IN8, the (130) and (001) reciprocal directions were within the horizontal scattering plane. [We quote the wave vector $Q = (H, K, L)$ in units of the tetragonal reciprocal lattice vectors $a^* = 2\pi/a = 2\pi/b = 1.63$ Å^{-1} and $c^* = 2\pi/c = 0.53$ Å^{-1} (a, b, and c are lattice parameters).] On 2T, an unconventional scattering geometry has been employed with the (100) and (011) reciprocal directions spanning the scattering plane. In both scattering geometries, in-plane wave vectors equivalent to (π, π) can be reached, with an out-of-plane wave vector component close to the maximum of the structure factor of low-energy excitations (*24*). In addition, wave vectors of the form $Q = (H, K, 1.7)$ around the

[1]Laboratoire Léon Brillouin, Commissariat à l'Energie Atomique–CNRS, CE Saclay, 91191 Gif sur Yvette, France. [2]Department of Physics, Princeton University, Princeton, NJ 08544, USA. [3]Département de Recherche Fondamentale sur la Matière Condensée, Commissariat à l'Energie Atomique Grenoble, 38054 Grenoble cedex 9, France. [4]CNRS–Centre de Recherches sur les Très Basses Températures, BP 166, 38042 Grenoble cedex 9, France. [5]Institut Laue-Langevin, 156X, 38042 Grenoble cedex 9, France. [6]Max-Planck-Institut für Festkörperforschung, 70569 Stuttgart, Germany.

*To whom correspondence should be addressed. E-mail: bourges@bali.saclay.cea.fr